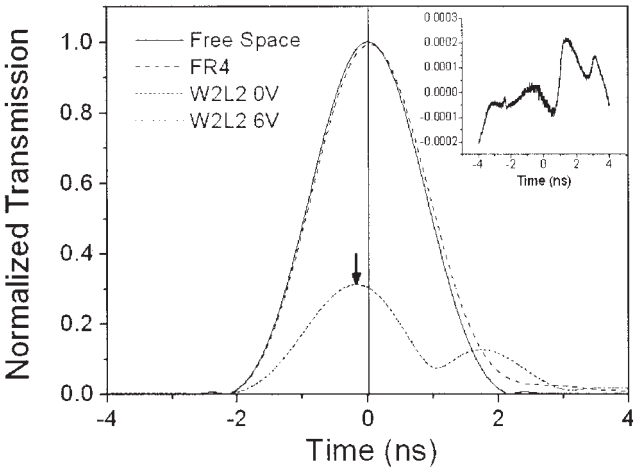

Figure 3 Pulse waveforms in the time domain. The solid line is the reference (incident) pulse, and the short dashed and dotted lines denotes the pulse train through power-OFF and power-ON OLEDs measured by the receiver, respectively. The dashed line denotes the result of the pulse passing through FR4 sample. The insert shows the difference between the power-ON and power-OFF cases (6V-0V)

electromagnetic wave does occur in the OLED sample. Hence, the superluminal effect may occur in the OLED sample as well. Next we examine the result of the time-domain transformation, using a pulse that includes the microwave range from 13.5 to 14.5 GHz through free space as a reference. The pulse through the power-off OLED sample was separated into two parts, as shown by the short dashed line in Figure 3. One of the pulse peaks was delayed by a time scale of 1.725 ns. On the other hand, another pulse peak was advanced by 0.183 ns with respect to the main peak of the pulse measured in free space, as shown by a downward arrow ($\downarrow$). Compared to the case of power-ON (6-V) OLED, this phenomenon is almost the same as the case of power-OFF OLED; the insert in Figure 3 shows the difference between these two cases. The thickness of the OLED sample (including the organic, cathode, and anode layers, but excluding the glass substrate and cap) was 355.8 nm. On the other hand, because the glass contributed a small delay ($\ll 0.1$ ns), and according to Eq. (2), the relation between the delay time and the optical path is given by

$$\Delta t = \frac{(n-1)L}{c}. \tag{2}$$

where the "effective" indices of refraction of the OLED sample for the two peaks were 1.45×10^8 and -1.54×10^7, respectively. The results of the measurement, phase advance, and peak splitting are amazing, and they provide a unique example of superluminality. However, the results of their deduction are even more astonishing. These results indicate: (i) a possible existence of negative-index materials; (ii) that the index is effectively extremely large. The existence of ultra-high indices of refraction may sound incredible; nevertheless, the ultra-high index has been employed previously in diffractive optics (that is, the Sweatt model) for modeling the diffractive optical surface [9]. This suggests that the OLED sample is effectively an "unusual" birefringence medium in the corresponding microwave range. The index is extremely large and the propagation has been greatly slowed down. By calculating the group velocity, we can deduce the values of the group velocity to be 2.06 and -19.5 m/s, respectively, which indicates that the group velocity has been slowed down, even to an order of seven, in comparison with the speed of light.

4. CONCLUSION

In conclusion, a novel high-speed-frequency electromagnetic characteristic of a power-OFF blue-light thin-film OLED sample has been reported. A superluminal phenomenon has been experimentally identified. The mechanism of this superluminal effect may be attributed to the fact that the OLED sample absorbs the energy and does not transfer it nonradiatively. Under this circumstance, the incident pulse can modulate the stored energy and induce the superluminality. However, a theoretical exploration remains to be done. The reported superluminal phenomenon occurs when the OLED sample is operated over an absorption band where anomalous dispersion occurs. It should be noted that different samples of OLEDs were also tested, and that the superluminal effects persist, provided that the OLED is operated over the absorption band and that anomalous dispersion occurs.

ACKNOWLEDGMENTS

The NCTU group thanks Y. C. Huang for his assistance with the experimental setup. This work is supported in part by the National Science Council of Taiwan, ROC, under contract no. NSC92-2112-M009-040.

REFERENCES

1. J.D. Jackson, Classical electrodynamics, 3rd ed., Wiley, New York, 1999.
2. G.P. Agrwall, Nonlinear fiber optics, 3rd ed., Academic Press, New York, 2001.
3. L. Brillouin, Wave propagation and group velocity, Academic Press, New York, 1960.
4. R. Loudon, The propagation of electromagnetic energy through an absorbing dielectric, J Phys A3 (1970), 233–245.
5. S. Chu and S. Wong, Linear pulse propagation in an absorbing medium, Phys Rev Lett 48 (1982), 738–741.
6. A. Dodabalapur, Organic light emitting diodes, Solid State Commu 102 (1997), 259–267.
7. A. Mikami, T. Koshiyama, and T. Tsubokawa, High-efficiency color and white-light polymer devices with high-index-of-refraction flexible plastic substrate, Soc Infor Display 2004 Symp Dig Technical papers (SID2004), Vol. 35, pp. 146–149.
8. D.M. Pozar, Microwave engineering, 2nd ed., Wiley, New York, 1998, p. 196.
9. W.C. Sweatt, Mathematical equivalence between a holographic optical element and an ultra-high index lens, J Optics Soc Am 69 (1979), 486–487.

SOLID-ANGLE FACTOR IN THE MAGNETIC-FIELD INTEGRAL EQUATION

Özgür Ergül and Levent Gürel
Department of Electrical and Electronics Engineering
Bilkent University
TR-06800, Bilkent
Ankara, Turkey

Received 18 November 2004

ABSTRACT: *The magnetic-field integral equation (MFIE) contains a geometry-dependent solid-angle factor due to the limit value of the magnetic field at the source region. Determination of the solid-angle factor*

becomes bewildering, especially at the points of geometric discontinuities caused by the simultaneous discretization of the MFIE and the geometry. In this paper, we clarify the ambiguity by scrutinizing the magnetic-field radiation integrals of the MFIE formulation. We prove that the solid-angle factor can be implicitly determined if the singular source-region magnetic-field expressions are correctly treated, thus eliminating the need for guessing or explicitly inserting solid-angle values in the formulation. © 2005 Wiley Periodicals, Inc. Microwave Opt Technol Lett 45: 452–456, 2005; Published online in Wiley InterScience (www.interscience.wiley.com). DOI 10.1002/mop.20851

Key words: *integral equation; magnetic-field; solid-style factor*

1. INTRODUCTION

The magnetic-field integral equation (MFIE) [1] is widely used in the solution of 3D scattering problems of conducting and closed surfaces via the method of moments (MOM) and the fast multipole method (FMM) discretized with the Rao–Wilton–Glisson (RWG) [2] functions defined on the triangular domains. Singularity-extraction methods applied on the MFIE integral provide accurate and efficient use of this equation [3, 4]. On the triangular (planar) surfaces, the expression for the self interactions reduces to an easy form, since the principle value of the scattered magnetic field is perpendicular to the plane of the current and, therefore, it is not tested. For the near-neighbor (touching) interactions, the extraction of the logarithmic singularity in the outer integrals provides sampling of the testing points, even at the edge of the basis triangles [5, 6].

The MFIE contains a solid-angle factor that depends on the geometrical features of the testing point sampled on the surface. The solid-angle factor has to be correctly determined for each testing point on the surface, which is usually discretized for numerical solutions. Such a discretization creates surface discontinuities marked by edges, where the magnetic field becomes singular. Prior to our recent work demonstrating how to test the singular magnetic fields on the edges accurately and efficiently [5, 7], the testing procedures commonly used in the literature have avoided the edges of the discretized surface, thus choosing the testing points strictly inside the piecewise planar subsurfaces, where the solid angle is simply 2π. On the other hand, since these locally planar subsurfaces are actually forming larger curved surfaces (for which the solid angle is not 2π), some studies in the literature [8] have proposed to explicitly insert a carefully guessed solid-angle factor for the planar-testing points in an effort to improve the accuracy of the MFIE. In this paper, we show that the solid-angle factor is implicitly and correctly accounted for through a proper handling of the near-neighbor interactions and that there is no need to insert explicitly or guess the solid-angle value. We have also observed some inherent inaccuracy in a specific implementation of the MFIE [6] that cannot be rectified by the correct use of the solid-angle factor. We will report our findings for improving the accuracy of the MFIE elsewhere [5, 7, 9].

2. LIMIT VALUE OF THE MFIE INTEGRAL

From the boundary condition for tangential magnetic field on the closed surface of a conducting scatterer, the MFIE can be written as

$$\boldsymbol{J}(\boldsymbol{r}) - \hat{\boldsymbol{n}} \times \int_S d\boldsymbol{r}'\boldsymbol{J}(\boldsymbol{r}') \times \nabla' g(\boldsymbol{r}, \boldsymbol{r}') = \hat{\boldsymbol{n}} \times \boldsymbol{H}^i(\boldsymbol{r}), \tag{1}$$

where the scattered magnetic field is expressed in terms of the induced (unknown) surface current $\boldsymbol{J}(\boldsymbol{r})$. In Eq. (1), the observation point $\boldsymbol{r}$ approaches the surface from the outside, $\hat{\boldsymbol{n}}$ is the outwardly directed normal, $\boldsymbol{H}^i(\boldsymbol{r})$ is the incident magnetic field, and

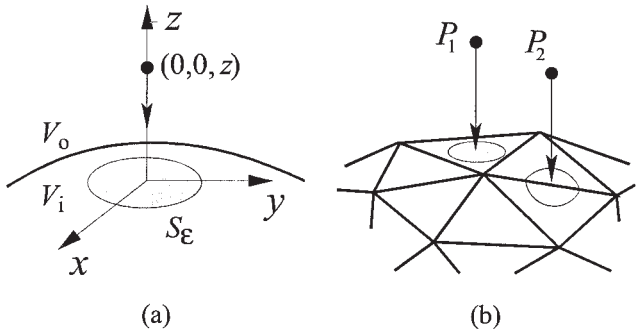

Figure 1 Observation points approaching (a) a smooth surface and (b) the smooth and discontinuous parts of a discretized surface

$$g(\boldsymbol{r}, \boldsymbol{r}') = \frac{e^{ikR}}{4\pi R} \quad (R = |\boldsymbol{r} - \boldsymbol{r}'|) \tag{2}$$

denotes the free-space Green's function in phasor notation with the $e^{-i\omega t}$ convention. The integral in Eq. (1) can be divided into two parts as

$$\boldsymbol{H}^s(\boldsymbol{r}) = \int_S d\boldsymbol{r}'\boldsymbol{J}(\boldsymbol{r}') \times \nabla' g(\boldsymbol{r}, \boldsymbol{r}') = \lim_{S_\varepsilon \to 0} \int_{S - S_\varepsilon} d\boldsymbol{r}'\boldsymbol{J}(\boldsymbol{r}') \times \nabla' g(\boldsymbol{r}, \boldsymbol{r}') + \lim_{S_\varepsilon \to 0} \int_{S_\varepsilon} d\boldsymbol{r}'\boldsymbol{J}(\boldsymbol{r}') \times \nabla' g(\boldsymbol{r}, \boldsymbol{r}'), \tag{3}$$

which can be written shortly as

$$\boldsymbol{H}^s(\boldsymbol{r}) = \boldsymbol{H}^s_{PV}(\boldsymbol{r}) + \boldsymbol{H}^s_{\varepsilon \to 0}(\boldsymbol{r}), \tag{4}$$

where PV denotes the principle value of the integral. As depicted in Figure 1, S_ε is the infinitesimal surface in the vicinity of the observation point, and the rest of the surface is taken into account by the first integral in Eq. (3). Even though in the limit S_ε shrinks to zero in Eq. (3), its contribution to the overall integral does not vanish since the integrand is singular as the observation point approaches the source distribution.

Figure 1(a) shows the observation point at (0, 0, z) approaching a smooth portion of the surface from the outside as z goes to zero. In this case, S_ε is locally planar in the shape of a circle with radius ε. Then, the Green's function can be approximated as

$$g(\boldsymbol{r}, \boldsymbol{r}') \approx \frac{1}{4\pi R} \tag{5}$$

and the second integral in Eq. (3) becomes

$$\boldsymbol{H}^s_{\varepsilon \to 0}(\boldsymbol{r}) = \lim_{S_\varepsilon \to 0} \int_{S_\varepsilon} d\boldsymbol{r}'\boldsymbol{J}(\boldsymbol{r}') \times \frac{\boldsymbol{R}}{4\pi R^3}, \tag{6}$$

where

$$\boldsymbol{R} = \boldsymbol{r} - \boldsymbol{r}' = \hat{\boldsymbol{z}}z - \hat{\boldsymbol{x}}x' - \hat{\boldsymbol{y}}y'. \tag{7}$$

If the current is continuous in the infinitesimal region, it can be assumed to be constant with the value of $\boldsymbol{J}_0 = \boldsymbol{J}(0, 0, 0)$, and

$$\boldsymbol{H}^s_{\varepsilon\to 0}(\boldsymbol{r}) = \boldsymbol{J}_0 \times \lim_{S_\varepsilon \to 0} \int_{S_\varepsilon} d\boldsymbol{r}' \frac{\boldsymbol{R}}{4\pi R^3}. \tag{8}$$

As the surface shrinks to zero, the integral can be evaluated as

$$\boldsymbol{H}^s_{\varepsilon\to 0}(\boldsymbol{r}) = \boldsymbol{J}_0 \times \frac{\hat{\boldsymbol{z}}}{2}. \tag{9}$$

This result can be generalized for all points on a smooth surface as

$$\boldsymbol{H}^s_{\varepsilon\to 0}(\boldsymbol{r}) = \boldsymbol{J}_0 \times \frac{\hat{\boldsymbol{n}}}{2} \tag{10}$$

and substituted back in Eqs. (3) and (1) to obtain

$$\frac{\boldsymbol{J}(\boldsymbol{r})}{2} - \hat{\boldsymbol{n}} \times \int_{S(PV)} d\boldsymbol{r}' \boldsymbol{J}(\boldsymbol{r}') \times \nabla' g(\boldsymbol{r}, \boldsymbol{r}') = \hat{\boldsymbol{n}} \times \boldsymbol{H}^i(\boldsymbol{r}). \tag{11}$$

If the surface is not smooth, then the situation P_2 illustrated in Figure 1(b) occurs as the observation point approaches a discontinuity of the surface with some external solid angle Ω_0. In the following sections, it will be shown that the evaluation of the integral in Eq. (8) will include terms involving Ω_0 for those situations. Indeed, even the 1/2 factor obtained in Eq. (9) for the smooth surface can be interpreted as $\Omega_0/4\pi$, where $\Omega_0 = 2\pi$ for a locally planar surface.

3. DISCRETIZATION OF THE MFIE

For the solution of the MFIE in Eq. (1) with MOM and FMM, we consider the discretization of the surface of the geometry by planar triangulation and the use of the RWG basis and testing functions on the planar triangular facets. That is, Eq. (1) can be discretized by expanding $\boldsymbol{J}(\boldsymbol{r})$ in a series of basis functions $\boldsymbol{b}_n(\boldsymbol{r})$, that is,

$$\boldsymbol{J}(\boldsymbol{r}) = \sum_{n=1}^{N} a_n \boldsymbol{b}_n(\boldsymbol{r}), \tag{12}$$

and by projecting the boundary condition (1) onto N testing functions $\boldsymbol{t}_m(\boldsymbol{r})$. Then, the $N \times N$ matrix equation is obtained as

$$\sum_{n=1}^{N} Z_{mn} a_n = v_m, \quad m = 1, \ldots, N, \tag{13}$$

where a_n is the unknown coefficient of the n^{th} basis function and Z_{mn} is the matrix element derived as

$$Z_{mn} = \int_{S_m} d\boldsymbol{r} \boldsymbol{t}_m(\boldsymbol{r}) \cdot \boldsymbol{b}_n(\boldsymbol{r}) - \int_{S_m} d\boldsymbol{r} \boldsymbol{t}_m(\boldsymbol{r}) \cdot \hat{\boldsymbol{n}} \times \int_{S_n} d\boldsymbol{r}' \boldsymbol{b}_n(\boldsymbol{r}') \times \nabla' g(\boldsymbol{r}, \boldsymbol{r}'). \tag{14}$$

Since the RWG basis and testing functions are defined on a pair of triangles sharing a common edge, they can be expressed as the sum of two half functions, that is,

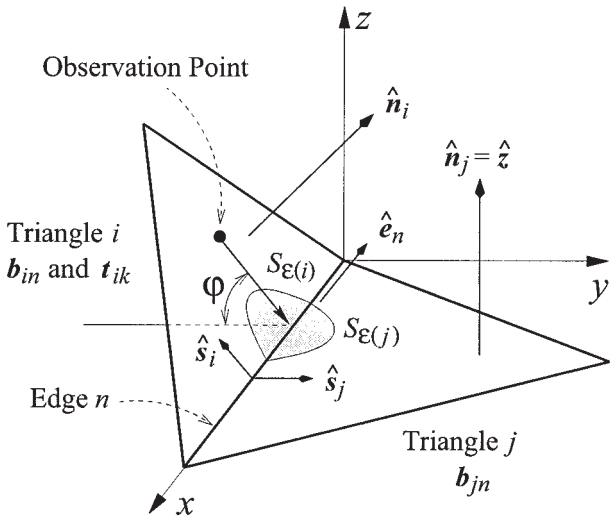

Figure 2 Observation point approaching the edge in the near-neighbor interaction

$$\boldsymbol{b}_n(\boldsymbol{r}) = \boldsymbol{b}_{in}(\boldsymbol{r}) + \boldsymbol{b}_{jn}(\boldsymbol{r}), \tag{15}$$

where the first and second subscripts denote the triangle index and edge index, respectively. In the self interaction of a half-function, the observation point is inside the basis triangle and the singularity-extraction methods applied with the limit procedures give [4]:

$$\int_{S_i} d\boldsymbol{r}' \boldsymbol{b}_{in}(\boldsymbol{r}') \times \nabla' g(\boldsymbol{r}, \boldsymbol{r}') = \frac{1}{2} \boldsymbol{b}_{in}(\boldsymbol{r}) \times \hat{\boldsymbol{n}}_i, \tag{16}$$

where $\boldsymbol{b}_{in}(\boldsymbol{r})$ represents the half-RWG basis function located on the i^{th} triangle and aligned with respect to the edge n, as shown in Figure 2. Therefore, for the self interaction of a half-function, the expression in Eq. (14) reduces to

$$Z_{ik,in} = \int_{S_i} d\boldsymbol{r} \boldsymbol{t}_{ik}(\boldsymbol{r}) \cdot \boldsymbol{b}_{in}(\boldsymbol{r}) - \frac{1}{2} \int_{S_i} d\boldsymbol{r} \boldsymbol{t}_{ik}(\boldsymbol{r}) \cdot \boldsymbol{b}_{in}(\boldsymbol{r}) = \frac{1}{2} \int_{S_i} d\boldsymbol{r} \boldsymbol{t}_{ik}(\boldsymbol{r}) \cdot \boldsymbol{b}_{in}(\boldsymbol{r}), \tag{17}$$

where $\boldsymbol{t}_{ik}(\boldsymbol{r})$ is the half-RWG testing function located on the i^{th} triangle with arbitrary alignment with respect to any one of its three edges, that is, k may or may not be equal to n. The expression in Eq. (17) is in accordance with Eq. (11), since the principle value in Eq. (11) is perpendicular to the planar current and not tested for the self interactions. Therefore, only the current term remains with 1/2 factor obtained in the limit procedure of the MFIE. For efficiency, the implementations are designed to ignore the inner integral for the self interactions and directly use the first term in Eq. (11) without performing any numerical integration procedures on the basis triangle.

The formulation in Eq. (11) assumes that the observation point is always located on the planar portions of the surface, as in the case of P_1 in Figure 1(b). On triangulated surfaces, this corresponds to sampling strictly inside the testing triangles for the near-neighbor interactions and thus avoiding to sample on the common edge between the basis and the testing triangles. Indeed, such a sampling strategy is usually preferred in the literature, since

the magnetic field has a logarithmic singularity at the edge of a basis triangle and the singularity is required to be tested when the testing and basis triangles are not on the same plane. On the other hand, a novel singularity-extraction method [5] applied on the outer integrals of the MFIE was recently introduced in order to accomplish testing on the edges of the basis triangles in a favorable manner [7]. Then, the question arises as how to modify the formulation for the case of P_2 in Figure 1(b) so that the solid angle of the surface is included in the calculations. In section 4, we show that if the formulation in Eq. (14) is used correctly, then the solid-angle factor of the MFIE is automatically and implicitly handled without having to insert it externally.

4. IMPLICIT COMPUTATION OF THE SOLID ANGLE

To demonstrate the implicit inclusion of the solid angle in the calculations, Figure 2 shows the case of near-neighbor interactions between the basis function $\boldsymbol{b}_n(\boldsymbol{r}) = \boldsymbol{b}_{in}(\boldsymbol{r}) + \boldsymbol{b}_{jn}(\boldsymbol{r})$ and the half-testing function $\boldsymbol{t}_{ik}(\boldsymbol{r})$ located on the i^{th} triangle with arbitrary alignment k. The half-basis-function $\boldsymbol{b}_{jn}(\boldsymbol{r})$ can further be decomposed as follows:

$$\boldsymbol{b}_{jn}(\boldsymbol{r}) = \hat{\boldsymbol{e}}_n b_{jn}^{(e)}(\boldsymbol{r}) + \hat{\boldsymbol{s}}_j b_{jn}^{(s)}(\boldsymbol{r}), \tag{18}$$

where $\hat{\boldsymbol{e}}_n$ and $\hat{\boldsymbol{s}}_j$ denote the directions that are parallel and perpendicular, respectively, to the edge n on the j^{th} triangle. We focus on the case when the observation point on the testing triangle approaches the common edge of the basis triangles on the x axis, that is, $R^0 \to 0$, where R^0 is the perpendicular distance to the edge. The angle between the approach path of the observation point and the x–y plane is φ. For this case, the $b_{jn}^{(e)}$ component of the current generates a singular magnetic field that is independent of φ. On the other hand, the $b_{jn}^{(s)}$ component of the current creates a nonsingular magnetic field that is a function of φ and, hence, a function of Ω_0. With the aid of the correction shown in [7], we obtain

$$\lim_{R^0\to 0}\left\{\lim_{S_{\varepsilon(j)}\to 0}\int_{S_{\varepsilon(j)}} d\boldsymbol{r}'\hat{\boldsymbol{s}}_j b_{jn}^{(s)}(\boldsymbol{r}')\times\nabla' g(\boldsymbol{r},\boldsymbol{r}')\right\} = \frac{\varphi}{2\pi} b_{jn}^{(s)}(\boldsymbol{r})\hat{\boldsymbol{s}}_j\times\hat{\boldsymbol{z}}, \tag{19}$$

where $S_{\varepsilon(j)}$ is the infinitesimal area of the j^{th} triangle around the limit location of the observation point. It should be noted that the expression in Eq. (19) is not explicitly calculated in an implementation, but it is automatically included in the calculation of the interaction between $\boldsymbol{b}_{jn}(\boldsymbol{r})$ and $\boldsymbol{t}_{ik}(\boldsymbol{r})$ using the second term of Eq. (14). If the half-basis-function on the i^{th} triangle is also considered, then

$$\lim_{R^0\to 0}\left\{\lim_{S_{\varepsilon(i)}\to 0}\int_{S_{\varepsilon(i)}} d\boldsymbol{r}'\hat{\boldsymbol{s}}_i b_{in}^{(s)}(\boldsymbol{r}')\times\nabla' g(\boldsymbol{r},\boldsymbol{r}')\right\} = \frac{1}{2} b_{in}^{(s)}(\boldsymbol{r})\hat{\boldsymbol{s}}_i\times\hat{\boldsymbol{n}}_i, \tag{20}$$

where $S_{\varepsilon(i)}$ is the infinitesimal portion of the i^{th} triangle. The expression in Eq. (20) is included in the first term of Eq. (14) and is automatically combined with (19) in the calculation of the interaction between the full-basis-function $\boldsymbol{b}_n(\boldsymbol{r})$ and the half-testing-function $\boldsymbol{t}_{ik}(\boldsymbol{r})$.

RWG functions enforce the continuity of the current perpendicular to the edge, that is,

$$b_{in}^{(s)}(\boldsymbol{r}) = -b_{jn}^{(s)}(\boldsymbol{r}) = b_n^{(s)}(\boldsymbol{r}) \tag{21}$$

as $\boldsymbol{r}$ approaches the edge. Also, note that

$$\hat{\boldsymbol{s}}_j\times\hat{\boldsymbol{z}} = -\hat{\boldsymbol{e}}_n \tag{22}$$

$$\hat{\boldsymbol{s}}_i\times\hat{\boldsymbol{n}}_i = \hat{\boldsymbol{e}}_n. \tag{23}$$

Using Eqs. (21)–(23), the magnetic field due to an infinitesimal surface around the edge of a full basis function can be obtained by adding Eqs. (19) and (20) as follows:

$$\lim_{R^0\to 0}\left\{\lim_{S_\varepsilon\to 0}\int_{S_\varepsilon} d\boldsymbol{r}'\hat{\boldsymbol{s}} b_n^{(s)}(\boldsymbol{r}')\times\nabla' g(\boldsymbol{r},\boldsymbol{r}')\right\} = \frac{\pi+\varphi}{2\pi} b_n^{(s)}(\boldsymbol{r})\hat{\boldsymbol{e}}_n, \tag{24}$$

where $S_\varepsilon = S_{\varepsilon(i)} \cup S_{\varepsilon(j)}$ and $\hat{\boldsymbol{s}}$ stands for $\hat{\boldsymbol{s}}_i$ and $-\hat{\boldsymbol{s}}_j$ in $S_{\varepsilon(i)}$ and $S_{\varepsilon(j)}$, respectively. In Eqs. (24), $\pi + \varphi$ represents the internal angle of the wedge formed by the i^{th} and j^{th} triangles. Then, the external solid angle spanned at the edge of the wedge is given by

$$\Omega_0 = 4\pi - 2(\pi + \varphi). \tag{25}$$

Finally, Eq. (24) can be evaluated as

$$\lim_{R^0\to 0}\left\{\lim_{S_\varepsilon\to 0}\int_{S_\varepsilon} d\boldsymbol{r}'\hat{\boldsymbol{s}} b_n^{(s)}(\boldsymbol{r}')\times\nabla' g(\boldsymbol{r},\boldsymbol{r}')\right\} = \left(1-\frac{\Omega_0}{4\pi}\right) b_n^{(s)}(\boldsymbol{r})\hat{\boldsymbol{e}}_n. \tag{26}$$

Hence, by combining the self and near-neighbor interactions of Eqs. (19) and (20), it is clear that the solid-angle dependence is correctly included in the MFIE. It should be emphasized that Eqs. (19) and (20) need not be computed explicitly, provided that the near-neighbor interactions (some of which involve singularities) are treated carefully [5, 7]. Then, the self interactions can still be calculated easily using Eq. (17), which will join the near-neighbor interactions to automatically account for the solid angle.

5. CONCLUSION

In this paper, the MFIE integral discretized with the RWG functions is analyzed in detail to show that the solid-angle factor of the MFIE is automatically included in the calculation of the near-neighbor interactions of the triangular subsurfaces, on the basis of which the RWG functions are defined. This demonstration is based on a careful evaluation of an analytical integral in the limit case, where the field tested at an observation point approaching the edge of the basis triangle is shown to be dependent on the angle between the approach path and the basis triangle. As a result, with the correct calculation of the MFIE integral, the need to guess and explicitly employ the solid-angle factor is eradicated.

ACKNOWLEDGMENTS

This work was supported by the Turkish Academy of Sciences in the framework of the Young Scientist Award Program (LG/TUBA-GEBIP/2002-1-12), by the Scientific and Technical Research Council of Turkey (TUBITAK) under Research Grant 103E008, and by contracts from ASELSAN and SSM.

REFERENCES

1. A.J. Poggio and E.K. Miller, Integral equation solutions of three-dimensional scattering problems, Computer Tech Electromagn R. Mittra (Ed.), Pergamon Press, Oxford, 1973, ch. 4.
2. S.M. Rao, D.R. Wilton, and A.W. Glisson, Electromagnetic scattering

by surfaces of arbitrary shape, IEEE Trans Antennas Propagat AP-30 (1982), 409–418.
3. R.D. Graglia, On the numerical integration of the linear shape functions times the 3-D Green's function or its gradient on a plane triangle, IEEE Trans Antennas Propagat 41 (1993), 1448–1455.
4. R.E. Hodges and Y. Rahmat-Samii, The evaluation of MFIE integrals with the use of vector triangle basis functions, Microwave Opt Technol Lett 14 (1997), 9–14.
5. L. Gürel and Ö. Ergül, Singularity of the magnetic-field integral equation and its extraction, IEEE Antennas Wireless Propagat Lett (to appear).
6. Ö. Ergül and L. Gürel, Investigation of the inaccuracy of the MFIE discretized with the RWG basis functions, 2004 IEEE AP-S Int Symp and URSI Radio Sci Mtg, Monterey, CA, 2004, pp. 3393–3396.
7. Ö. Ergül and L. Gürel, Improved testing of the magnetic-field integral equation, IEEE Microwave Wireless Comp Lett (to appear).
8. J.M. Rius, E. Úbeda, and J. Parrón, On the testing of the magnetic field integral equation with RWG basis functions in method of moments, IEEE Trans Antennas Propagat 49 (2001), 1550–1553.
9. Ö. Ergül and L. Gürel, Improving the accuracy of the MFIE with the choice of basis functions, 2004 IEEE AP-S Int Symp and URSI Radio Sci Mtg, Monterey, CA, 2004, pp. 3389–3392.
10. N. Morita, N. Kumagai, and J.R. Mautz, Integral equation methods for electromagnetics, Artech House, Boston, 1990.

INTEGRATION OF A FLUORESCENCE DETECTION SYSTEM AND A LAMINATE-BASED DISPOSABLE MICROFLUIDIC CHIP

Rudi Irawan,[1] Tjin Swee Chuan,[2] and Fu Chit Yaw[1]
[1] Biomedical Engineering Research Centre
School of Electrical and Electronic Engineering
Nanyang Technological University
Singapore 639553
[2] Photonics Research Centre
School of Electrical and Electronic Engineering
Nanyang Technological University
Singapore 639798

Received 12 November 2004

ABSTRACT: *A fluorescence-detection system for immunoassay applications in a laminate-based microfluidic chip has been developed and tested. Blue-LED, plastic fiber, CCD detector, mylar-D, and fluorescein are used as an excitation source, a light coupler, a fluorescence detector, a microfluidic substrate, and a sample, respectively. The system is able to detect from 1 to 1000 μg/L fluorescein. A method to avoid cross talk is also presented.* © 2005 Wiley Periodicals, Inc. Microwave Opt Technol Lett 45: 456–460, 2005; Published online in Wiley InterScience (www.interscience.wiley.com). DOI 10.1002/mop.20852

Key words: *fluorescence; microfluidic chip; cross-talk*

1. INTRODUCTION

The performance of quantitative immunoassays is largely restricted to centralized laboratories because of the need for long assay times and complex and expensive equipment, as well as a highly trained operator. If a wider range of immunoassays could be run in a simpler manner, more inexpensively, and at the point of care or in the home-health-care setting, the health of millions of patients could be improved annually. To achieve this objective, a simple, compact, smart, and inexpensive device providing high-quality results is required.

Immunoassay is an analytical method that is widely used in clinical diagnoses, environmental analyses, and biochemical studies because of its extremely high selectivity and sensitivity [1]. There are many types of optical techniques which are commonly used for biosensing applications. Fluorescence-based sensors are the most highly developed due to their high sensitivity, versatility, accuracy, and fairly good selectivity [2, 3]. The fluorescence method is also very suitable for miniaturization [4–6].

In clinical practices, the problem of very small sample volume is often faced. Microfluidic technology is ideal for handling costly and difficult-to-obtain samples and reagents, because it requires only a very small sample volume, on the order of μL or even nL. Microfluidic channel dimensions typically range from 1 to 1000 μm in width and height [7]. The miniaturization of chemical reactions to the microfluidic system leads to a reduction of reagent volume, a decrease in analysis time, and the capability of carrying on simultaneous analyses of different analytes.

Besides the commonly used glass and silica wafers, polymer-based materials such as polydimethylsiloxene (PDMS), polymethyl-methacrylate (PMMA), and polycarbonate [8–11] have been introduced recently as microfluidic materials. Thin laminate sheets, such as Mylar, have a very good seal characteristic and are nonporous solid, so they do not absorb the biomolecule sample [11]. Microfluidic channels based on laminate can be fabricated easily through molding, embossing, and casting processes [7, 9, 11, 12], while other materials may need to use the time-consuming photomask-generation, photolithography, and etching processes, which hamper the rapid turnaround of the new design. In this paper, microchannels on Mylar-D were fabricated for less than an hour using a direct-write CO_2 laser system. This paper describes the development of the integration of a fluorescence-detection system and a microfluidic chip fabricated with Mylar-D and demonstrates the performance of the device. This developed system serves as a platform for developing a multichannel fluorescence point-of-care immunoassay system.

2. EXPERIMENTAL

2.1. Microfluidic Chip Fabrication

In this experiment, 300-μm-width channels were machined using the ablation process in which a CO_2 laser cutting machine was focused on a two-layer Mylar sheet, producing a channel cross section of 100×300 μm. The tops and bottoms of the channels were capped using 50-μm-thick Mylar-D sheets. Each channel has an inlet and an outlet port assessed by Nanoport assemblies and drug-delivery tubes.

2.2. Sample Preparation

Fluorescein from Sigma-Aldrich Laborchemikalien Gmbh, Seeize, was used as a sample for testing the system. Fluorescein is used because it is widely available, inexpensive, and commonly used as a biomolecular-fluorescence tag. The samples were diluted inside phosphate-buffered saline (PBS) of pH 7.4. The samples were driven into the microchannels by a microfluidic pump through the inlet ports of the microchannels.

2.3. Optical Fluorescence Detection System

A 470-nm blue LED from Nichia, Tokushima, was used as an excitation source. The emission spectrum of this LED covers the excitation peak of fluorescein, about 490 nm. The light beam from this LED was focused into 250-μm plastic optical fiber and then directed onto the microchannel in a Mylar sheet. The fluorescence emission of fluorescein was collected by a high-NA objective lens (mounted on a micromanipulator) and then focused by a convex